Critical mode and band-gap-controlled bipolar thermoelectric properties of SnSe

I. Loa,[1,*] S. R. Popuri,[2] A. D. Fortes,[3] and J. W. G. Bos[2,†]

[1]*SUPA, School of Physics and Astronomy, and Centre for Science at Extreme Conditions, The University of Edinburgh, Edinburgh EH9 3FD, United Kingdom*

[2]*Institute of Chemical Sciences and Centre for Advanced Energy Storage and Recovery, School of Engineering and Physical Sciences, Heriot-Watt University, Edinburgh EH14 4AS, United Kingdom*

[3]*ISIS Facility, STFC Rutherford Appleton Laboratory, Harwell Oxford, Didcot, Oxon OX11 0QX, United Kingdom*

(Received 10 November 2017; published 13 August 2018)

The reliable calculation of electronic structures and understanding of electrical properties depends on an accurate model of the crystal structure. Here we have reinvestigated the crystal structure of the high-zT thermoelectric material tin selenide, SnSe, between 4 and 1000 K using high-resolution neutron powder diffraction. Symmetry analysis reveals the presence of four active structural distortion modes, one of which is found to be active over a relatively wide range of more than ±200 K around the symmetry-breaking *Pnma-Cmcm* transition at 800 K. Density functional theory calculations on the basis of the experimental structure parameters show that the unusual, steplike temperature dependencies of the electrical transport properties of SnSe are caused by the onset of intrinsic bipolar conductivity, amplified and shifted to lower temperatures by a rapid reduction of the band gap between 700 and 800 K. The calculated band gap is highly sensitive to small out-of-plane Sn displacements observed in the diffraction experiments. SnSe with a sufficiently controlled acceptor concentration is predicted to produce simultaneously a large positive and a large negative Seebeck effect along different crystal directions.

DOI: 10.1103/PhysRevMaterials.2.085405

I. INTRODUCTION

Recently, single crystals of the binary compound tin selenide, SnSe, were reported to exhibit exceptionally good thermoelectric properties [1–3]. The discovery of high thermoelectric efficiency in a "simple" bulk material has added to the renewed interest in thermoelectric materials for energy harvesting applications, where waste heat is converted directly to electricity in reliable, low-maintenance semiconductor devices. The high performance in SnSe arises from the combination of an ultralow lattice thermal conductivity and a rapid increase in the thermoelectric power factor with temperature above 600 K. The low thermal conductivity has been attributed to highly anharmonic lattice dynamics [4–8], whereas the unusual, almost steplike changes of the electrical conductivity and Seebeck coefficient around 700 K have remained largely unexplained [9–17].

The crystal structure of SnSe can be described as a highly distorted rock-salt derivate [18–20]. Above 800 K, the structure has space group symmetry *Cmcm* and features rock-salt-type double layers, see Figs. 1(a) and 2(a). Upon cooling below 800 K, the structure undergoes a displacive phase transition to lower symmetry *Pnma*. Instead of space group *Cmcm*, we will use henceforth the nonstandard setting *Bbmm*, so as to keep the crystal axes in the same orientation as for *Pnma* [21]. The electronic structure and transport properties of SnSe were investigated in several computational studies in the framework of density functional theory (DFT) [9–17], revealing a complex arrangement of anisotropic bands that contribute to the electrical transport. Surprisingly, none of these studies considered the gradual variation of the crystal structure with temperature. Most commonly, only the crystal structures in the low- and high-temperature limit (typically ∼300 and ∼800 K) were used. Although much insight has been gained from these investigations, a calculation of the electronic structure and transport properties directly from the temperature-dependent crystal structure data is missing.

Here we present a reinvestigation of the crystal structure of SnSe, extending the temperature range to 4–1000 K, using high-resolution neutron powder diffraction and symmetry mode analysis to determine the active structural order parameters. This structural information is then used to follow the evolution of the electronic structure of SnSe as a function of temperature using DFT calculations. These reveal a direct correlation between the primary order parameter and the electronic band gap; they show that small atomic displacements have a profound effect on the electronic structure, and they provide a coherent explanation for the unusual temperature dependence of the experimentally observed transport properties. We will also discuss the possibility of realizing simultaneously a large positive and negative Seebeck effect along different directions of a single crystal.

II. TECHNIQUES

SnSe was synthesized as described previously [22]. Neutron powder diffraction data were collected on a 10-g sample on

*Corresponding author: I.Loa@ed.ac.uk
†j.w.g.bos@hw.ac.uk

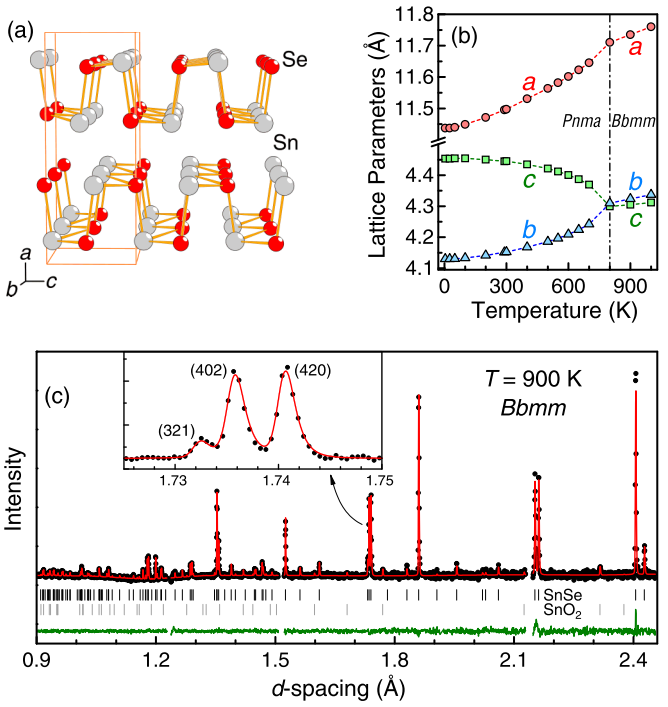

FIG. 1. (a) Crystal structure of SnSe below 800 K in the *Pnma* setting. (b) Temperature dependence of the lattice parameters of SnSe. (c) Neutron powder diffraction pattern of SnSe at 900 K (*Bbmm* phase) and Rietveld fit. Measured data are shown by black circles, the Rietveld fit by red lines, and the difference curve by the green line at the bottom. Tick marks show the fitted peak positions for SnSe (black, upper row) and a ∼1 wt.% SnO_2 impurity that was also observed (gray, lower row). Three small regions in *d* spacing with artifacts from the TOF detection were excluded from the fits.

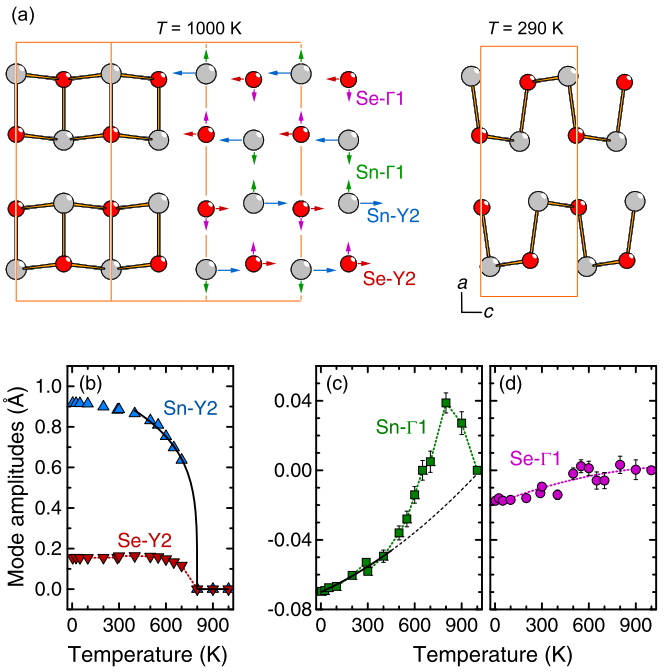

FIG. 2. (a) Atomic displacement patterns of the active symmetry-adapted distortion modes of SnSe. The arrows are not to scale. (b)–(d) Amplitudes of the distortion modes as a function of temperature, see text for details. Solid black lines in (b) and (c) are fits to the data as explained in the text, the dashed line in (c) shows a quadratic extrapolation of the 4–400 K data, and the dotted lines in (b)–(d) are guides to the eye.

the time-of-flight (TOF) high resolution powder diffractometer (HRPD), equipped with a He-flow cryostat (4–290 K) and furnace (300–1000 K), at the ISIS spallation neutron source, Rutherford Appleton Laboratory, UK. High-temperature patterns were collected in a vacuum-sealed (10^{-5}bar) quartz tube to avoid sublimation of SnSe at high temperatures. The diffraction patterns are not affected by texturing and enable the determination of accurate atomic coordinates and thermal displacement parameters. Structural refinements using the Rietveld method were carried out with the GSAS program [23–25].

Electronic structure calculations were performed in the framework of density functional theory (DFT) and the full-potential augmented-plane-wave + local orbital (APW+lo) approach as implemented in the WIEN2K code [25,26]. Exchange and correlation effects were treated with the revised generalized gradient approximation for solids (PBEsol) [27] in the total-energy calculations, and the modified Becke-Johnson potential by Tran and Blaha [28] was used in the band structure and band gap calculations. Spin-orbit coupling was found to have a negligible effect on the band structure and was therefore not included. From the electronic band structures, electrical transport properties were calculated in the framework of Boltzmann transport theory as implemented in the BOLTZTRAP code [25,29].

III. RESULTS AND DISCUSSION

A. Crystal structure

The structural parameters of SnSe in the temperature range of 4–1000 K were obtained from Rietveld refinements. Figure 1(c) shows an example of a diffraction pattern and Rietveld fit, and more extensive data are presented in the Supplemental Material [25], including all structural parameters in tabulated form. The temperature dependence of the lattice parameters [Fig. 1(b)] is in line with previous results [18–20,30–32]. All axes show gradual changes up to ∼600 K, followed by more rapid changes up to the phase transition at ∼800 K. The *b* and *c* parameter approach each other with increasing temperature, and they are reversed in length from 800 K onwards. A noteworthy detail is illustrated in the inset of Fig. 1(c): The doublet of the (402) and (420) reflections of the high-temperature phase is clearly split, thereby demonstrating unambiguously that the metric remains orthorhombic, contrary to a previous report [30]. The evolution of the positional parameters with temperature (see Supplemental Material [25]) confirms the symmetry-raising transition from the *Pnma* to the *Bbmm* (*Cmcm*) space group symmetry at ∼800 K [18–20]. Our refined structural parameters are consistent with those reported recently by Sist *et al.* [31] (x-ray powder diffraction) and Serrano-Sánchez *et al.* [32] (neutron powder diffraction) but covering a wider temperature range (Fig. S4 in the Supplemental Material [25]).

In order to characterize the phase transition further, we found it helpful to consider not the bare fractional atomic

coordinates, but instead the *symmetry-allowed distortion modes* [33]. These describe the shifts of the equilibrium atomic positions relative to the high-temperature, high-symmetry structure. The amplitudes of these distortions were determined as a function of temperature from the refined structure parameters using the ISODISTORT software [33], and the high-symmetry, 1000-K structure was used as the reference. By convention, each mode amplitude is defined as the sum of the displacements of all displaced atoms in the unit cell, added in quadrature. For all distortion modes considered here, the mode amplitude is twice the displacement of an individual atom.

Four modes were found to be active during the *Bbmm-Pnma* transition: the $Y2$ and $\Gamma 1$ modes of both Sn and Se. The atomic displacement patterns of these distortion modes and the variation of the fitted mode amplitudes with temperature are shown in Fig. 2. The $Y2$ modes correspond to shifts parallel to SnSe layers (and in-phase within each double layer), whereas the $\Gamma 1$ modes describe motions perpendicular to the layers which are antiphase within each double layer.

By far the largest change in amplitude was observed for the Sn-$Y2$ mode, see Fig. 2(b). In the 400–1000 K range, the Sn-$Y2$ amplitude shows critical behavior with a transition temperature T_s of 800 K and an exponent $\beta = 0.23(1)$ (solid black line). The amplitude of the Se-$Y2$ distortion mode is ∼5 times smaller than that of Sn-$Y2$. Interestingly, the Sn-$\Gamma 1$ mode with atomic displacements perpendicular to the layers exhibits a pronounced anomaly around the transition temperature [Fig. 2(c)]: A slightly superlinear increase in mode amplitude from 4–400 K is followed by a rapid increase up to $T_s = 800$ K, and an equally rapid decrease at higher temperature. Quadratic extrapolation of the low-temperature behavior reproduces the experimental 1000-K data point, supporting the notion of anomalous behavior from ∼400 up to 1000 K. For completeness, the Se-$\Gamma 1$ mode amplitude exhibits a small steady variation over the whole 4–1000 K interval [Fig. 2(d)].

In summary, the symmetry analysis shows that the motion of the Sn and Se atoms during the *Pnma-Bbmm* transition can be decoupled into independent, symmetry-adapted displacements parallel and perpendicular to the SnSe double layers. It identifies the Sn-$Y2$ mode as a primary order parameter for the phase transition, corresponding to a large Sn displacement within the double layers [Fig. 2(b)]. Upon heating, this displacement starts to become significant above 600 K and saturates at 800 K, consistent with the early work by von Schnering and Wiedemeier [19].

The symmetry analysis reveals furthermore anomalous Sn displacements perpendicular to the rock-salt layers (Sn-$\Gamma 1$ mode), which have not been recognized in previous studies [19,20,30–32]. They occur over a wide temperature interval around the phase transition at 800 K. This mode anomaly affects mainly the shortest Sn-Se bond distance (see the Supplemental Material [25]). We will demonstrate below that this structural detail has a significant effect on the electronic properties.

B. Electronic structure

We now turn to the DFT calculations, which were performed in order to understand how the structural variations of SnSe with temperature affect the electronic structure and transport properties. The modified Becke-Johnson (mBJ) exchange and correlation potential [28] was employed here in order to overcome the well-known problem that DFT calculations with standard LDA and GGA potentials significantly underestimate semiconductor band gaps. For the ambient-temperature crystal structure, the band structure calculated here with the mBJ potential is in close agreement with results obtained previously in GW calculations [10,11], which aim specifically at describing the electronic excitation spectrum correctly. The calculated band structure is also consistent with photoemission data [34]. The band structure calculations were then performed using the structural parameters measured between 4 and 1000 K.

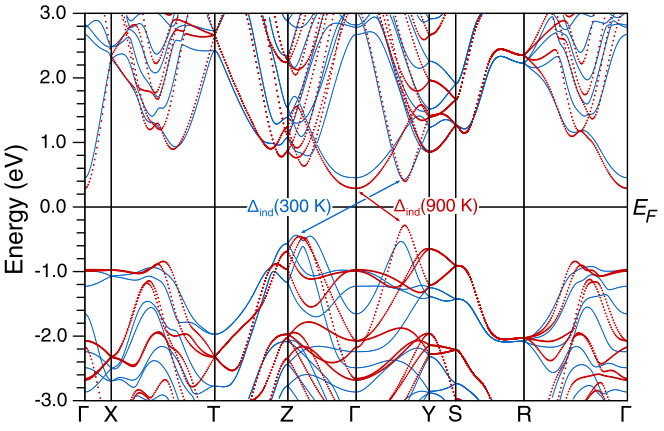

FIG. 3. Calculated band structure of SnSe at 300 K (solid lines, blue) and 900 K (dotted lines, red). The special points refer to the *Pnma* Brillouin zone, which was used for both calculations to allow for a direct comparison.

The calculated band structure shows significant qualitative changes across the *Pnma-Bbmm* transition, with most of the changes occurring between 700 and 800 K. In these calculations, SnSe remains an indirect semiconductor at all temperatures, but the locations of the valence band maximum and the conduction band minimum change during the transition, as illustrated in Fig. 3. It should be noted, however, that details such as the exact relative energies of band extrema become less relevant with increasing temperature because the Fermi-Dirac distribution broadens, so that the electrical transport properties result increasingly from an average over many bands.

Figure 4(a) shows that the calculated band gap decreases with increasing temperature, following the primary order parameter (Fig. 5). In addition, the effect of the seemingly small Sn-$\Gamma 1$ distortion mode on the band gap is profound: When the anomaly of this mode around 800 K is suppressed [dashed line in Fig. 2(c)], a further reduction of the band gap by 80 meV at 800 K is obtained. Figure 4(b) illustrates that suppressing the peak in the Sn-$\Gamma 1$ amplitude around 800 K also has significant effect on the total energy: it increases by up to ∼18 meV per formula unit. Both effects demonstrate how very sensitively the electronic structure responds to details of the crystal structure.

It is therefore important to bear in mind that the band structure calculations were performed assuming a static crystal lattice, as is common practice [9–17]. However, the thermal motion of the atoms at the high temperatures of interest

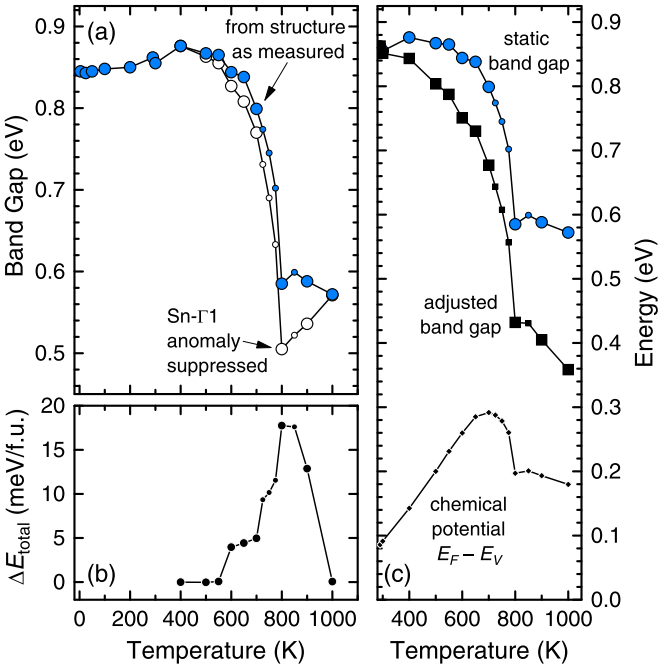

FIG. 4. (a) Evolution of the calculated indirect band gap of SnSe with temperature. Solid symbols show results based on the crystal structure as measured, and open symbols where the peak of the Sn-Γ1 distortion mode around 800 K was suppressed [dashed line in Fig. 2(c)]. The band gap is that of the static lattice. Small symbols represent additional computational results where interpolated structural parameters were used. (b) Difference in total energy between that of the hypothetical structure with the Sn-Γ1 anomaly suppressed and that of the crystal structure as measured. (c) Static band gap and gap adjusted for thermal motion after [35], and chemical potential E_F relative to the valence band maximum E_V for an extrinsic hole concentration of $n_p = 5\times10^{17}\text{cm}^{-3}$.

for thermoelectrics will affect the band gap and thus the transport properties. For the following calculations of transport properties, we adjusted the calculated band gap above room temperature by $-0.30\,\text{meV/K}$ based on the experimental results by Parenteau and Carlone [35] so as to obtain a realistic estimate of the high-temperature band gap [Fig. 4(c)]; see the Supplemental Material [25] for full details. A full *ab initio* calculation of the temperature dependence of the band gap is desirable, but it would require an accurate modeling of the anharmonic lattice dynamics [4–7] and its effect on the electronic structure—a formidable task beyond the scope of this work.

C. Transport properties

Figure 6(a) shows the calculated temperature dependence of the conductivity along the three orthorhombic crystal axes ($a, b, c \rightarrow xx, yy, zz$), normalized by the electron scattering time τ. The extrinsic hole concentration was chosen as $n_p = 5\times10^{17}\text{cm}^{-3}$ at 300 K as suggested by Hall effect data by Zhao *et al.* [1], and the number of extrinsic holes per unit cell was assumed to remain constant at higher temperatures. The calculated conductivity shows a very pronounced anisotropy in the 300–600 K range, a steep, steplike increase in a narrow range from 600 to 800 K, and a more moderate increase with

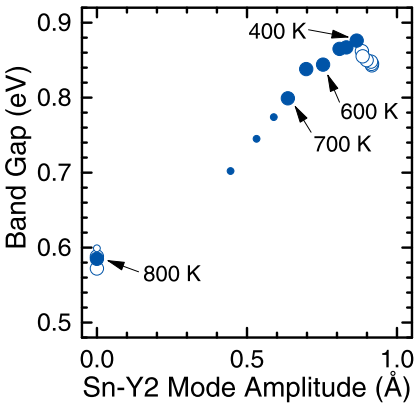

FIG. 5. Correlation of the calculated band gap of SnSe with the amplitude of the Sn-$Y2$ critical mode. Open symbols mark data points below 400 K and above 800 K; small symbols indicate results where interpolated structural parameters were used in the calculations.

temperature above 800 K. Overall, these results compare well with the experimental results for the single-crystal conductivity by by Zhao *et al.* [1], see Fig. 6(c).

These computational results explain the unusual steplike increase in conductivity in SnSe between 600 and 800 K as well as the marked kink at 800 K [1]. The conductivity starts to increase along with the increased carrier concentration at the onset of intrinsic bipolar conductivity, as expected, but this gradual process is *amplified and shifted to lower temperatures* by the rapid reduction of the band gap between 700 and 800 K (Fig. 4). The structural transition and the associated rapid

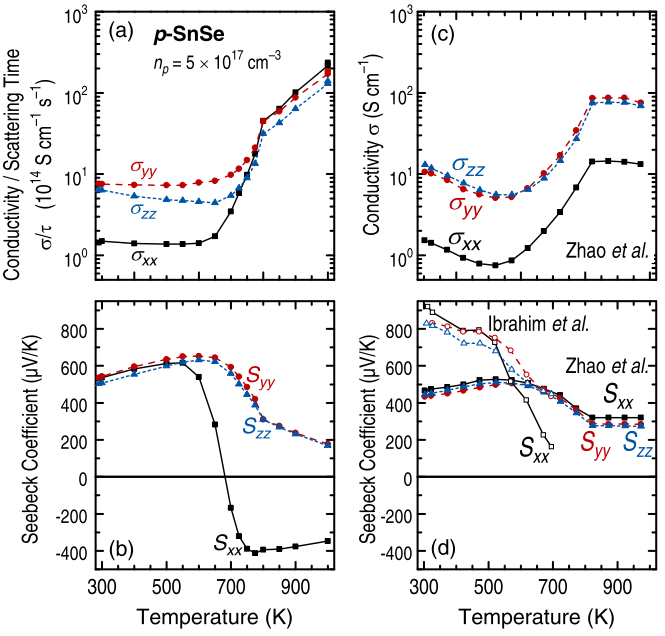

FIG. 6. (a) Calculated electrical conductivity σ divided by the scattering time τ of p-SnSe and (b) calculated Seebeck coefficient as a function of temperature. A hole-doping concentration of $n_p = 5\times10^{17}\text{cm}^{-3}$ at ambient temperature and the adjusted band gaps from Fig. 4(c) were used in both cases. (c) and (d) Corresponding experimental results by Zhao *et al.* [1] (solid symbols) and Ibrahim *et al.* [36] (open symbols).

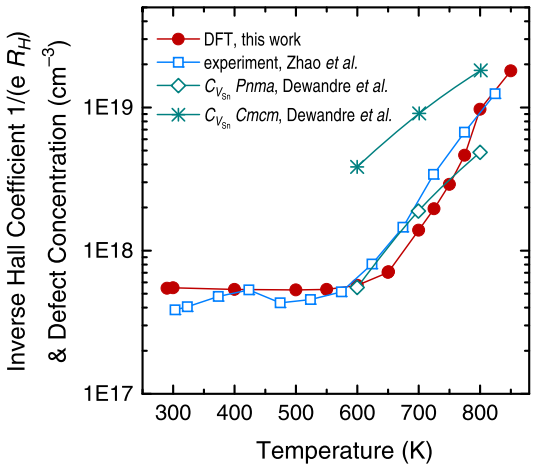

FIG. 7. Inverse Hall coefficients $1/(eR_H)$ and Sn vacancy concentrations $C_{V_{Sn}}$ in SnSe as a function of temperature. Red solid circles show the average inverse Hall coefficient obtained here from Boltzmann transport calculations assuming hole-doping concentration of $n_p = 5\times10^{17}\text{cm}^{-3}$ at ambient temperature and the adjusted band gaps from Fig. 4(c). Blue open squares show the corresponding experimental data by Zhao *et al.* [1]. Cyan diamonds and stars show the carrier concentration obtained from the Sn^{2-} vacancy model by Dewandre *et al.* [13] for the *Pnma* and *Cmcm*/*Bbmm* phases, respectively.

reduction of the band gap are completed at 800 K, giving rise to the marked change in slope of the conductivity. As noted above, the calculated conductivity is with respect to the scattering time τ, which generally decreases with increasing temperature and will hence reduce somewhat the rise in conductivity above 800 K. A notable difference between the computational and experimental results is the apparent disappearance of the anisotropy at high temperature in the calculations. The calculated conductivity is normalized with respect to the electron scattering τ, and a significant difference between the in-plane and out-of-plane electron scattering times would recover the experimentally observed anisotropy in the conductivity.

We performed additional calculations that show that the results for the temperature dependence of the electrical conductivity do not depend qualitatively on details of the underlying band structures (Figs. 5(a) and 6(a) in the Supplemental Material [25]): (i) If the as-calculated band structures without band-gap adjustment on account of thermal motion are used, the results remain qualitatively the same; the reduced change in band gap leads only to a smaller increase in conductivity. (ii) The results also remained largely unchanged in calculations in which the same, fixed 300-K band structure together with the adjusted band gaps from Fig. 4(c) was used. In this scenario, the effective masses and relative order of band extrema are fixed. The key conclusion is therefore that the unusual temperature dependence of the conductivity is controlled by the variation of the band gap (via the associated variation of the charge carrier concentration), which in turn correlates with the Sn-$Y2$ critical mode (Fig. 5), but not by the details of the band shapes, i.e., the effective masses and relative order of band extrema.

As a further test of the calculations and the above conclusions, we compare in Fig. 7 the average inverse Hall coefficient $1/(eR_H)$ from the measurements by Zhao *et al.* [1] and from our calculations. These measures of the effective charge carrier concentration are in very good agreement over the whole temperature range, which confirms the view that the steep increase in conductivity follows the increase in charge carrier concentration at the onset of intrinsic conductivity at ∼600 K, where the band gap also starts to decrease.

The above conclusions are in contrast to the recently advanced notion that the carrier concentration in SnSe is dominated by the thermal creation of Sn vacancies [13]. In the study by Dewandre *et al.*, the standard semiconductor behavior discussed above, i.e., the thermal excitation of electrons from the valence to the conduction band states and the associated intrinsic, bipolar conductivity were not considered. Instead, the formation energies of a number of intrinsic defects (vacancies, interstitial atoms, Sn/Se exchange) were determined in DFT-based calculations. The activation energy of the lowest-energy defect, the Sn vacancy ($V_{Sn}^{(2-)}$) was found to be close to an activation energy (0.67 eV) that describes the variation in carrier concentration between 600 and 800 K, as deduced from the inverse Hall coefficient by Zhao *et al.* [1] (Fig. 7). Based on the similarity of the activation energy and Sn^{2-} vacancy formation energy, the rise in carrier concentration between 600 and 800 K was attributed to the creation of additional Sn vacancies.

We would like to point out that in a bulk semiconductor, the creation of a Sn vacancy (V_{Sn}) requires the creation of at least one secondary defect in order to conserve the bulk stoichiometry. For example, the Sn ion removed during the creation of a Sn vacancy could move to an interstitial site, creating a secondary interstitial defect (Sn_{Int}), or occupy a Se site together with Se moving to an interstitial site ($Sn_{Se} + Se_{Int}$). Consequently, the effective activation energy will be substantially higher than for the Sn vacancy alone, which is by far the lowest-energy defect considered in [13], and the creation of free charge carriers by this mechanism will be exponentially suppressed compared to the results by Dewandre *et al.* (reproduced in Fig. 7). Even though thermal activation of defects will undoubtedly occur at sufficiently high temperatures with respect to the effective activation energies, we conclude that this mechanism can neither explain the observed complex variation of the electrical conductivity (or free carrier concentration) with temperature, nor is it necessary.

Figure 6(b) shows the calculated Seebeck coefficient as a function of temperature for temperature gradients along the three crystal directions. The results for the directions *b* and *c* parallel to the crystal layers (S_{yy}, S_{zz}) are in excellent agreement with the experimental results by Zhao *et al.* [1] between 300 and 800 K. At higher temperatures, the calculations yield a continued gradual decrease of the Seebeck coefficient with increasing temperature, whereas experimental studies found the Seebeck coefficient to be temperature independent above 800 K [1,37]. A possible explanation for this and the corresponding deviation for the conductivity is that the band gap assumes a minimum value at ∼800 K and increases slightly thereafter up to 1000 K, similar to what we observed by suppressing the small anomaly in the Sn-Γ1 distortion mode [Fig. 4(a)]. Such an effect may well arise from the anharmonic atomic motion, but it would require extensive modeling to test this hypothesis. Unlike the electrical conductivity, the Seebeck coefficient and its temperature dependence are sensitive to details of the band

structure beyond the band gap [25] as discussed previously [9,10].

The computational results for S_{xx}, in the direction perpendicular to the layers, deviate from the experimental results by Zhao *et al.* [1]. We obtained a much more pronounced reduction of the Seebeck coefficient and a change in sign at 680 K. Around 800 K, the calculations yield a large negative Seebeck coefficient of $S_{xx} \approx -400\,\mu$V/K, i.e., with a larger absolute value than for the b and c directions. Similar results were also obtained in other recent computational studies [9,10], but their relevance (see below) was perhaps not fully appreciated. As discussed previously [9,10], the negative sign of S_{xx} is a result of bipolar conductivity in SnSe above 700 K. The magnitude of the band gap is therefore an important factor [34], and the agreement of our calculations with the experimental results for the electrical conductivity and inverse Hall coefficient and their temperature dependencies indicates that the temperature-dependent band gap used here is realistic. The result of a negative S_{xx} is a rather robust outcome of several calculations, despite significant variations with respect to the band shapes and band gaps, and this result should not simply be rejected because it is at variance with the experimental results by Zhao *et al.* [1]. In fact, in a recent single-crystal transport study up to 700 K by Ibrahim *et al.* [36], a rapid reduction in S_{xx} above 500 K was reported, and the data are suggestive of a change in sign at around 750 K [Fig. 6(d)]. And in a study on polycrystalline samples, a rapid reduction of the Seebeck coefficient was observed above 600 K, decreasing down to $\sim 145\,\mu$VK^{-1} at 960 K [38]. The polycrystalline average of positive and negative Seebeck coefficients would explain such a low value.

These experimental results not only lend support to our computational results, they also highlight the limitations and inconsistencies of the currently available experimental data. Our computational work is based on the assumption that the extrinsic carrier concentration remains constant in the 300–1000 K range, which implies that the acceptors are shallow impurities, as has generally been assumed. A possible explanation for the differences in the transport properties in different studies is the existence of deep acceptors in some samples, which could lead to substantial differences in the extrinsic carrier concentration and hence transport properties at high temperatures. A reexamination of the single-crystal transport properties of SnSe above 700 K, and also the influence of different acceptor types, would be extremely valuable. Controlling the defect concentration and keeping it below $\sim 10^{18}$ cm^{-3} would be crucial for observing the negative S_{xx} Seebeck effect.

The prediction of a large Seebeck effect with opposite signs along two directions of a bulk crystal may seem very unusual, but there are precedents for such behavior: Early work on bismuth suggests a change in sign along one crystal direction at 280 °C [39], and nominally undoped, p-type Bi_2Te_3 has been reported to show Seebeck coefficients with opposite signs between 240 and 390 °C, which was attributed to bipolar conductivity [40].

The simultaneous occurrence of a positive and negative Seebeck effect in highly anisotropic, layered materials at the onset of bipolar conduction is an interesting new aspect that could be exploited in thermoelectric applications. It would eliminate the need to find suitable dopants to produce both p- and n-type versions of a given compound. Instead, a single, highly anisotropic material could be used in different orientations, i.e., parallel and perpendicular to the layers. Such a material does not necessarily need to be single crystalline, a highly oriented polycrystalline material [41] would be sufficient and preferable in terms of production cost and mechanical properties.

IV. CONCLUSIONS

Our reexamination of the structural phase transition in SnSe using high-resolution powder neutron diffraction and symmetry-mode analysis identifies Sn displacements parallel to the SnSe layers (Sn-$Y2$ mode) as a primary order parameter and provides evidence for anomalous Sn displacements perpendicular to the rock-salt layers (Sn-$\Gamma 1$ mode) that have profound effect on calculated electronic properties. The magnitude of the band gap is directly related to the Sn-$Y2$ mode amplitude during the transition. The magnitude of the calculated band gap was found to be sensitive to the atomic coordinates so that simulations based on DFT-relaxed crystal structures do not work sufficiently well in SnSe—a limitation that probably applies more generally to materials with anharmonic, soft chemical bonds.

The transport property calculations provide a coherent explanation of the unusual steplike variation of the electrical conductivity observed experimentally in SnSe [1]. This behavior originates from the onset of intrinsic bipolar conductivity, amplified and shifted to lower temperatures by the rapid reduction of the band gap between 700 and 800 K. The calculated thermopower becomes highly anisotropic at temperatures above 600 K, and SnSe is predicted show simultaneously large positive and negative Seebeck coefficients along different crystal directions. This prediction is consistent with one experimental study limited to 700 K [38], but at variance with another [1]. On the experimental side, it may prove important to control the concentration of deep defects in SnSe [35,42] so as to avoid an increase of the extrinsic carrier concentration above room temperature. It is worthwhile to identify in future research highly anisotropic materials with simultaneously large positive and negative Seebeck effects as a possible route towards more efficient thermoelectric materials.

Supporting data are available from the University of Edinburgh's DataShare repository [43].

ACKNOWLEDGMENT

S.R.P. and J.W.G.B. acknowledge the EPSRC (EP/N01717X/1), Leverhulme Trust (RPG-2012-576), and the STFC for provision of beam time #1520262 at ISIS [44].

[1] L.-D. Zhao, S.-H. Lo, Y. Zhang, H. Sun, G. Tan, C. Uher, C. Wolverton, V. P. Dravid, and M. G. Kanatzidis, Nature (London) **508**, 373 (2014).

[2] C. Chang, M. Wu, D. He, Y. Pei, C.-F. Wu, X. Wu, H. Yu, F. Zhu, K. Wang, Y. Chen, L. Huang, J.-F. Li, J. He, and L.-D. Zhao, Science **360**, 778 (2018).

[3] Z.-G. Chen, X. Shi, L.-D. Zhao, and J. Zou, Prog. Mater. Sci. **97**, 283 (2018).

[4] C. W. Li, J. Hong, A. F. May, D. Bansal, S. Chi, T. Hong, G. Ehlers, and O. Delaire, Nat. Phys. **11**, 1063 (2015).

[5] D. Bansal, J. Hong, C. W. Li, A. F. May, W. Porter, M. Y. Hu, D. L. Abernathy, and O. Delaire, Phys. Rev. B **94**, 054307 (2016).

[6] J. M. Skelton, L. A. Burton, S. C. Parker, A. Walsh, C.-E. Kim, A. Soon, J. Buckeridge, A. A. Sokol, C. R. A. Catlow, A. Togo, and I. Tanaka, Phys. Rev. Lett. **117**, 075502 (2016).

[7] J. Hong and O. Delaire, arXiv:1604.07077.

[8] S. R. Popuri, M. Pollet, R. Decourt, M. L. Viciu, and J. W. G. Bos, Appl. Phys. Lett. **110**, 253903 (2017).

[9] K. Kutorasinski, B. Wiendlocha, S. Kaprzyk, and J. Tobola, Phys. Rev. B **91**, 205201 (2015).

[10] G. Shi and E. Kioupakis, J. Appl. Phys. **117**, 065103 (2015).

[11] R. Guo, X. Wang, Y. Kuang, and B. Huang, Phys. Rev. B **92**, 115202 (2015).

[12] G. Ding, G. Gao, and K. Yao, Sci. Rep. **5**, 9567 (2015).

[13] A. Dewandre, O. Hellman, S. Bhattacharya, A. H. Romero, G. K. H. Madsen, and M. J. Verstraete, Phys. Rev. Lett. **117**, 276601 (2016).

[14] A. J. Hong, L. Li, H. X. Zhu, Z. B. Yan, J.-M. Liu, and Z. F. Ren, J. Mater. Chem. A **3**, 13365 (2015).

[15] B. Xu, J. Zhang, G. Yu, S. Ma, Y. Wang, and L. Yi, J. Electron. Mater. **45**, 5232 (2016).

[16] J. Yang, G. Zhang, G. Yang, C. Wang, and Y. X. Wang, J. Alloys Compd. **644**, 615 (2015).

[17] H. Mori, H. Usui, M. Ochi, and K. Kuroki, Phys. Rev. B **96**, 085113 (2017).

[18] H. Wiedemeier and F. J. Csillag, Z. Kristallogr. **149**, 17 (1979).

[19] H. G. von Schnering and H. Wiedemeier, Z. Kristallogr. **156**, 143 (1981).

[20] T. Chattopadhyay, J. Pannetier, and H. von Schnering, J. Phys. Chem. Solids **47**, 879 (1986).

[21] I. Loa, R. J. Husband, R. A. Downie, S. R. Popuri, and J.-W. G. Bos, J. Phys.: Condens. Matter **27**, 072202 (2015).

[22] S. R. Popuri, M. Pollet, R. Decourt, F. D. Morrison, N. S. Bennett, and J. W. G. Bos, J. Mater. Chem. C **4**, 1685 (2016).

[23] A. C. Larson and R. B. von Dreele, GSAS: General Structure Analysis System. Report LAUR 86-748, Los Alamos National Laboratory, NM, USA, 1986.

[24] B. H. Toby, J. Appl. Crystallogr. **34**, 210 (2001).

[25] See Supplemental Material at http://link.aps.org/supplemental/10.1103/PhysRevMaterials.2.085405 for details.

[26] P. Blaha, K. Schwarz, G. K. H. Madsen, D. Kvasnicka, and J. Luitz, *Wien2k: An Augmented Plane Wave + Local Orbitals Program for Calculating Crystal Properties* (K. Schwarz, Techn. Universität Wien, Austria, 2001).

[27] J. P. Perdew, A. Ruzsinszky, G. T. Csonka, O. A. Vydrov, G. E. Scuseria, L. A. Constantin, X. Zhou, and K. Burke, Phys. Rev. Lett. **100**, 136406 (2008).

[28] F. Tran and P. Blaha, Phys. Rev. Lett. **102**, 226401 (2009).

[29] G. K. H. Madsen and D. J. Singh, Comput. Phys. Commun. **175**, 67 (2006).

[30] K. Adouby, C. Pérez-Vicente, J. C. Jumas, R. Fourcade, and A. Abba Touré, Z. Kristallogr. **213**, 343 (1998).

[31] M. Sist, J. Zhang, and B. Brummerstedt Iversen, Acta Cryst. B **72**, 310 (2016).

[32] F. Serrano-Sánchez, N. M. Nemes, O. J. Dura, M. T. Fernandez-Diaz, J. L. Martínez, and J. A. Alonso, J. Appl. Crystallogr. **49**, 2138 (2016).

[33] B. J. Campbell, H. T. Stokes, D. E. Tanner, and D. M. Hatch, J. Appl. Crystallogr. **39**, 607 (2006).

[34] C. W. Wang, Y. Y. Y. Xia, Z. Tian, J. Jiang, B. H. Li, S. T. Cui, H. F. Yang, A. J. Liang, X. Y. Zhan, G. H. Hong, S. Liu, C. Chen, M. X. Wang, L. X. Yang, Z. Liu, Q. X. Mi, G. Li, J. M. Xue, Z. K. Liu, and Y. L. Chen, Phys. Rev. B **96**, 165118 (2017).

[35] M. Parenteau and C. Carlone, Phys. Rev. B **41**, 5227 (1990).

[36] D. Ibrahim, J.-B. Vaney, S. Sassi, C. Candolfi, V. Ohorodniichuk, P. Levinsky, C. Semprimoschnig, A. Dauscher, and B. Lenoir, Appl. Phys. Lett. **110**, 032103 (2017).

[37] L. Zhang, J. Wang, Q. Sun, P. Qin, Z. Cheng, Z. Ge, Z. Li, and S. Dou, Adv. Energy Mater. **7**, 1700573 (2017).

[38] S. Sassi, C. Candolfi, J.-B. Vaney, V. Ohorodniichuk, P. Masschelein, A. Dauscher, and B. Lenoir, Appl. Phys. Lett. **104**, 212105 (2014).

[39] R. W. Boydston, Phys. Rev. **30**, 911 (1927).

[40] J. H. Dennis, Adv. Energy Convers. **1**, 99 (1961).

[41] H. Guo, H. Xin, X. Qin, J. Zhang, D. Li, Y. Li, C. Song, and C. Li, J. Alloys Compd. **689**, 87 (2016).

[42] A. Agarwal, S. H. Chaki, S. G. Patel, and D. Lakshminarayana, J. Mater. Sci.: Mater. Electron. **5**, 287 (1994).

[43] University of Edinburgh's DataShare repository, http://datashare.is.ed.ac.uk, doi:10.7488/ds/2401.

[44] STFC ISIS Facility, Experiment #1520262, J.-W. G. Bos *et al.* (2015), doi:10.5286/ISIS.E.63527800.